

Formation of Highly Oriented Cellulose Nanocrystal Films by Spin Coating Film from Aqueous Suspensions

Mingzhe Jiang¹, S. Nicole DeMass¹, D. Ross Economy², Thomas Shackleton¹ and Christopher L. Kitchens^{1*}

¹Department of Chemical and Biomolecular Engineering, Clemson University, Clemson, South Carolina, USA 29634

²Department of Material Science & Engineering, Clemson University, Clemson, South Carolina, USA 29634

Received March 25, 2016; Accepted September 22, 2016

ABSTRACT: Spin coating was used to cast a uniform film of cellulose nanocrystals with low surface roughness and variable thickness as a function of operational parameters that include rotational speed and dispense suspension concentration. The film thickness was controllable from 40 nm up to 1 μm with surface roughness an order of magnitude less than blade-coating methods. The degree of radial orientation was qualitatively assessed and shown to be variable with processing parameters. Under specific processing conditions, the formation of striation patterns was observed and associated with film drying instability. The striation patterns are periodic in nature where the wavelength and amplitude are controllable to a certain degree with wetting film concentration and rotational speed. The striation patterns possess ordered, oriented nanorods, which exist as both rippled ring-like structures and radial ridges along the shear direction. There is potential to employ these rippled structures as low-cost manufacturing of ordered materials, device platforms, or optical components such as diffraction gratings. Mechanical properties of the films were measured by nanoindentation. The maximum elastic modulus of the films was 8.3 GPa and the maximum hardness was 322 MPa. A post-drying heat treatment (80 °C) was employed and resulted in a 17% increase in modulus and 35% increase in hardness, which is attributed to the formation of an enhanced intermolecular hydrogen bonding network between nanocrystals with removal of bound water.

KEYWORDS: Cellulose nanocrystal, spin coating film, striations, birefringence

1 INTRODUCTION

Cellulose is desirable for applications of many materials because it is an inexpensive and abundant polymer with many useful characteristics, including biodegradability, biocompatibility, nontoxicity, mechanical strength, and optical properties, owing to liquid crystal formation [1–3]. For microscale structures or device fabrication, the use of cellulose nanocrystals (CNCs) in high performance coatings is attractive, largely due to the anisotropic, or rod-shaped geometry [4]. In general, the possibility to control the architecture of two- and three-dimensional arrays of nanomaterials is critical in many applications such as ordered nanomaterial films [5], electronics, and optical devices [6]. The same can be stated about the emerging possibility of CNCs as building blocks for a broad range of applications such as biosensors [7], solar cells [8], and other

potential device platforms [4]. In such cases, the additional benefits of improved mechanical characteristics with aligned CNCs to yield directional properties can also be realized.

The CNC films have been produced by solution-casting, spin-coating [9–12], blade-coating [13], and Langmuir-Blodgett techniques [14]. Of the different methods, spin coating stands out as a promising technique due to the high surface uniformity and controllable film thickness [6]. Films of desirable surface uniformity and thickness can be obtained by changing various control parameters such as wetting film concentration, rotational speed, ramp rate, spin time, solid support, deposition speed, humidity, and temperature [15–18]. However, despite being a well-developed technique, there are a limited number of works discussing the application of spin coating to CNC films. Prior works associated with CNC films have focused on the casting of monolayer or multi-layer CNC films and the coverage of CNCs on the substrate at low concentration. Most of the film thicknesses are below 100 nm and the wetting film concentration is

*Corresponding author: ckitch@clermson.edu

DOI: 10.7569/JRM.2016.634131

below 50 mg/ml, which exists in the isotropic phase of the suspension. Thus, a more extensive study characterizing a larger range of CNC film thicknesses using a single-step spin-coating process is required to determine the full potential of CNC film processing and overcome the narrow range of processing conditions in previous studies. For many device and film type applications, it is desirable to achieve film thicknesses that are on the order of 1 μm with low surface roughness, which are intermediate between spin-coating and blade-coating techniques.

The thickness, homogeneity, and structure of complex solution films are governed by many factors, including the solvent volatility, solution viscoelastic properties, and constituent properties [19]. For most solutions, a balance is established between viscous outward radial solution flow on the substrate surface and solvent evaporation from the coating solution. Meyerhofer [20] analyzed this dual action process by splitting the spin-coating run into two stages—one dominated by viscous flow and the second dominated by evaporation. With this approach he was able to predict the final coating thickness, H , in terms of several key solution parameters, according to

$$H = x \left[\frac{C\sqrt{\omega}}{2(1-x)\frac{\rho\omega^2}{3\eta}} \right]^{1/3} \quad (1)$$

where x is the initial mass fraction of the coating solution, ω is the rotation rate, ρ is the solution density, η is the viscosity, and C is a proportionality constant that depends on whether airflow above the surface is laminar or turbulent and the diffusivity of solvent molecules in air (since it is limited by the diffusion of the evaporating molecules through the aerodynamic boundary layer above the surface of the wafer during spinning). It is noticed that H is inversely related to the square root of the rotation rate in the model. Although the model might not apply to colloidal systems, this power law relationship between rotation rate and the thickness still remains [21]. Furthermore, since CNC suspensions are shear thinning fluids [3], the power law behavior might have exponential variations at different concentrations [22]. These together contribute to our understanding and determination of the optimal operating parameters in film processing.

In many cases, films formed by spin coating are substantially more uniform across the entire substrate than other coating methods, however, certain surface defects can occur. Striations have been observed with spin coating of polymers and photoresists, but are often considered undesirable surface

defects [23–25]. These surface striations can be manifested in different geometries. One appears as thickness undulations or “ripples” that are perpendicular to the radial direction. A second is “radial ridges” that emanate spoke-like from the center of the substrate in the radial direction. In other cases, the center of the substrate can display a cellular thickness pattern reminiscent of Bénard cells, which result from instabilities but do not result in striations [26]. The actual mechanism by which striations develop during the spin-coating process is not totally understood, although there have been demonstrated links between solvent evaporation during the thinning process and the development of these particular surface defects [27, 28]. As an alternative to categorizing these striations as undesirable defects, there is potential to take advantage of this phenomenon as a low-cost and automatic formation of surface patterns for applications in textured surfaces, devices and sensors [29].

In this study, a systematic examination was performed on the spin coating of CNC aqueous suspensions into uniform films. While the importance of substrate material selection or an anchoring agent to modulate the substrate-film interactions in the spin-coating process has been recognized, this work focuses on the operational spin-coating parameters (e.g., rotational speed and dispense concentration) which are included in the basic spin-coating model [20]. The shear-induced radial orientation of the CNCs with thickness- and surface roughness-dependent processing parameters was investigated. Unexpectedly, the formation of rippled and radial ridge striation patterns was observed and associated with film drying instability under specific spinning conditions. Moderate control of the ripple feature sizes was achieved with spin-coating parameters, which may have potential implications in device fabrication.

2 EXPERIMENTAL

2.1 Spin Coating

Aqueous CNC suspensions were prepared by controlled sulfuric acid hydrolysis of cellulose filter paper by previously published methods [3]. The initial concentration of the suspensions after preparation was 16 mg/ml. In order to reach higher concentrations, the suspensions were gently stirred in an open beaker, evaporating the water at room temperature and pressure. The concentration was measured by thermal gravimetric analysis (TGA), using a TA Instruments SDT-Q600. Samples with concentrations ranging from 93 to 172 mg/ml (listed in Table 1) were used in this study, which are noticeably higher than previous studies. Two-inch diameter silicon wafers purchased from

University Wafer Inc., with <100> orientation, were used as the spin-coating substrate. The silicon wafer substrate was treated with piranha solution to produce a hydrophilic surface of comparable mechanical properties, thus negating the need for anchoring agents to promote substrate-film interactions. The wafers were cleaned prior to spin coating by sonicating in a DI water bath for 10 minutes and then soaking in piranha solution in a water bath at 75 °C for 1 hour. After removing the wafers from the piranha solution, the wafers were washed and cleaned with DI water in a sonication bath for another 20 minutes and stored in beakers of DI water.

Prior to spin coating, the wafers were removed from the DI water and dried with an air gun. Spin coating was conducted on a Laurell Technologies WS-650-23 spin coater. The wafers were set and centered on the spin-coating stand to begin the spin-coating process, starting with a water pretreatment step. Initially, DI water (1 ml) was dynamically dispensed onto the wafers 3 seconds into a 15 second spin step at 800 rpm and an 800 rpm/s acceleration to wet the wafer surface. Then, the CNC suspension was dispensed on the wafer surface. For the lower concentrations used, the CNC suspension easily wetted the entire silicon substrate at rotation speed, while for concentrations greater than 147 mg/mL, the high viscosity required excess solution to achieve complete coverage of the substrate. In order to reach the full coverage of CNCs wetting film on wafer surface, 600 µL of the aqueous CNC suspension was dispensed 3 seconds into a 10 second step at 1000 rpm and an acceleration of 1000 rpm/s. This volume of CNC suspension was chosen in order to fully wet the wafer without significant excess. After the coating suspension was applied, a 25 second spin step of varying rotational speeds between 1000 rpm and 8000 rpm and an acceleration of 1000 rpm/s was used to obtain films of different thicknesses. The film was then dried using a final spin step at 1000 rpm with an acceleration of 100 rpm/s for 5 minutes. This was found to be the most effective spin protocol for obtaining uniform coverage of the wafers with a dry CNC film over the concentration range. Table 1 details the parameters investigated.

All the casted films have full coverage on the wafer surface.

2.2 Film Characterization

The dried CNC film thickness and roughness were measured using an Olympus LEXT OLS4000 3D laser measuring microscope. Using the laser imaging mode at a magnification from 5X to 100X (with a 5 nm z-direction resolution limit), 3D images of the wafer were obtained at various points on the wafer. Three images each were taken at the center of the wafer (inside of 5 mm from the wafer center), in the middle of the wafer (between 5 mm and 20 mm from the wafer center), and at the edge of the wafer (between 20 mm and 25 mm from the wafer center). Images were taken on lines scored through the CNC film with a metal needle to the wafer surface from the wafer center to the edge. The film thickness was determined by taking a line roughness measurement perpendicular to the scratch and measuring the height difference between the wafer and film surfaces. The roughness of the film was calculated by taking an average surface roughness measurement of the image in an area without the scratch.

The CNC sample films were characterized with an Olympus BX-60 optical polarized light microscope in reflective mode. Pictures were taken at 5X to 20X magnification between polarized films at room temperature (23 °C). Polarized light microscopy with a first-order retardation plate was used to observe birefringent films and characterize optical axis and orientation. The first-order retardation plate is useful for enhancing contrast in weakly birefringent specimens. When a birefringent specimen with a wavefront ellipsoid parallel to the retardation plate is inserted into the optical pathway, the blue and green wavelengths are elliptically polarized and interfere at the intermediate image plane to form a hue similar to second-order blue. When a birefringent specimen has a wavefront ellipsoid perpendicular to the retardation plate, elliptically polarized green and red wavelengths ultimately recombine to form a first-order yellow interference color. A high amount of single color distribution in the

Table 1 Samples conducted under different conditions.

Concentration mg/ml	Rotational speed (rpm)									
	1000	2000	2500	3000	3500	4000	5000	6000	7000	8000
93	X	X		X		X	X			
125	X	X			X	X	X			
147		X	X	X		X	X	X	X	
172		X			X		X		X	X

images indicates a high level of orientation order of the film. Scanning electron microscopy (SEM) images of the film surface were acquired with a Hitachi S-4800 field-emission scanning electron microscope (FESEM) operating at 2 kV, magnification from 750X to 200,000X, and a working distance of 5.7 mm.

Nanoindentation testing was performed using a Hysitron Triboscope with Digital Instruments multimode atomic force microscope (AFM) base and diamond Berkovich indentation probe to test the CNC film hardness and bulk modulus. The instrument was calibrated using a fused quartz standard and validated both before and after testing. Four indentations were taken at four different maximum loads for a total of 16 tests on each sample (150, 200, 250, 300 μN). Indentation spacing was a minimum of 10 μm between each test location to ensure a negligible influence of pre-existing deformation zones and was shallower than 150 nm to minimize effects of the underlying substrate. Oliver-Pharr analysis was used to determine the resulting hardness and bulk elastic modulus from the nanoindentation measurements [30].

3 RESULTS AND DISCUSSION

3.1 Spin Coating of CNC Films

To produce films of different thicknesses in the 100 nm to 1 μm range, the CNC suspension concentration and the spinning rate were varied. In Figure 1, a trend of decreasing thickness with increasing rotational speed is shown over all concentrations. At 93 mg/ml,

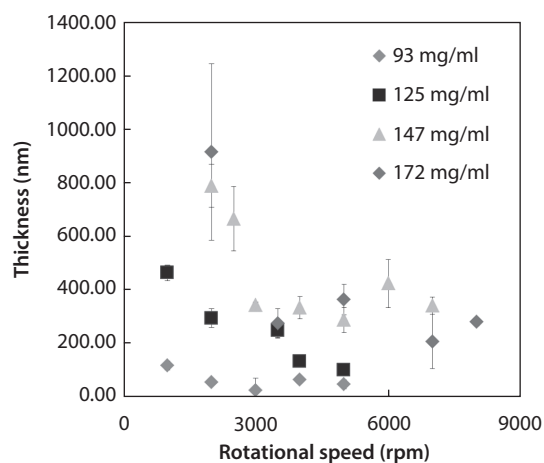


Figure 1 Film thickness vs. rotational speeds at CNC concentrations of 93 mg/mL (circles), 125 mg/mL (squares), 147 mg/ml (triangles), and 172 mg/ml (diamonds). The error bars represent the standard deviation of five replicate measurements.

a maximum film thickness of 130 nm is achieved at 1000 rpm and a plateau of 50 nm is reached at rotational speeds above 2500 rpm. At 125 mg/ml, a maximum film thickness of 500 nm is achieved at 1000 and plateaus at ≈ 100 nm at rotational speeds above 4000 rpm. Both 147 mg/ml and 172 mg/ml show similar trends of thickness change versus rotational speed, the maximum thickness is above 800 nm at 2000 rpm and plateaus at ≈ 200 to 400 nm when the rotational speed is above 4000 rpm. Increased variability (indicated by the error bars) in thickness measurement is observed for the higher concentrations compared to 93 mg/ml and 125 mg/ml. It is likely that at a certain rotational speed level, the spin-coating process enters into an evaporation control stage which can induce additional variability [31]. The wetting film can become "solid-like," where the movement of the film becomes negligible even when the rotational speed is increased. The thickness plateau at higher rotational speed agrees with power law behavior of the thickness vs. rotational speed in the colloidal system, which is $h_f \sim \omega^{-b}$. Applying power law fitting to the experimental data gives a power law exponent at different concentrations, which are listed in Table 2. When the concentration is at 93 mg/ml, the exponent has a value close to 0.5, which is in the range predicted by Rehg and Higgins [21] for colloidal suspensions. According to our previous study [3], when the CNC concentration is higher than 96 mg/ml, the suspension transits from well-dispersed colloidal system into high shear-thinning fluids and liquid crystal phase. When the concentration is above 125 mg/ml, the exponent value is close to 0.8, which agrees with shear-thinning fluid spin-coating predictions [22].

The variability in thickness measurement is paralleled by the area surface roughness measurements, as shown in Figure 2. At 93 mg/ml, the surface roughness is below 20 nm for all rotational speeds; this result together with low error bars indicates a relatively stable and uniform surface formation of the CNC film. When the concentration is equal to or above 125 mg/ml, the general trend is that surface roughness decreases and levels off with increasing rotational speed at a given

Table 2 Power law exponent of the concentration vs. thickness measurements.

Cellulose nanocrystal concentration	Power law exponent, b	R ²
93 mg/ml	0.442	0.69
125 mg/ml	0.871	0.86
147 mg/ml	0.734	0.65
172 mg/ml	0.849	0.70

concentration. However, given the variability in surface roughness measurement, indicated by the standard deviation, only generalized trends are apparent where the surface roughness trends with film thickness. Statistical analysis and ANOVA t-test indicates that the roughness values over all spin speeds for the 93 mg/ml are statistically different from the other concentrations within a 95% confidence interval, while

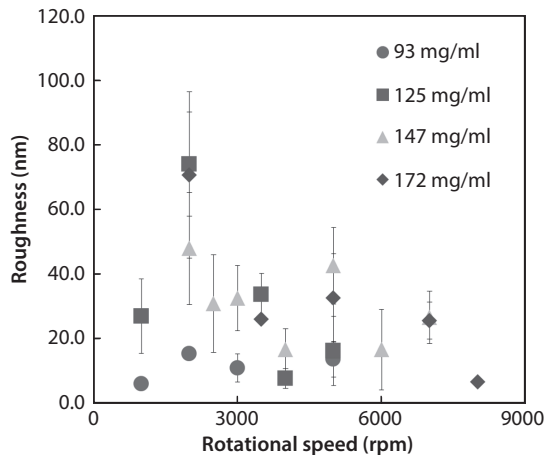


Figure 2 Area surface roughness vs. rotational speeds at CNC concentrations of 93 mg/mL (circles), 125 mg/mL (squares), 147 mg/mL (triangles), and 172 mg/mL (diamond). The error bars represent the standard deviation of five replicate measurements.

the roughness values for the 125, 147, and 172 mg/ml concentrations are not statistically different within the 95% confidence interval. This distinction is also in line with the results from the power law analysis and can also be attributed to viscous effects. Overall, the minimum roughness is achieved at the highest rotational speeds and is below 20 nm for all 4 concentrations.

3.2 CNC Film Anisotropic Property and Surface Structure Formation

Due to the anisotropic geometry of CNCs and their co-operative orientation into liquid crystal phases, it is possible to prepare oriented cellulose films in response to shear [13, 32]. CNC alignment in the radial direction arises from the viscous shear as the suspension flows outward during spin coating. Kontturi *et al.* [10] studied the effects of substrate and CNC concentration on the film thickness for low concentrations (0.125 to 20 mg/ml). In this concentration regime, the CNC suspension exists as an isotropic phase and nanorod alignment induced by shear force is negligible. Higher concentrations (93 to 172 mg/ml, which covers the range of biphasic region and liquid crystal regions) were chosen for this study and result in different trends. At 147 mg/ml, the oriented surface of the spin-coated dried films display a color change from blue to yellow as the sample stage is rotated 90° (Figure 3a,b), indicating that the nanocrystals are

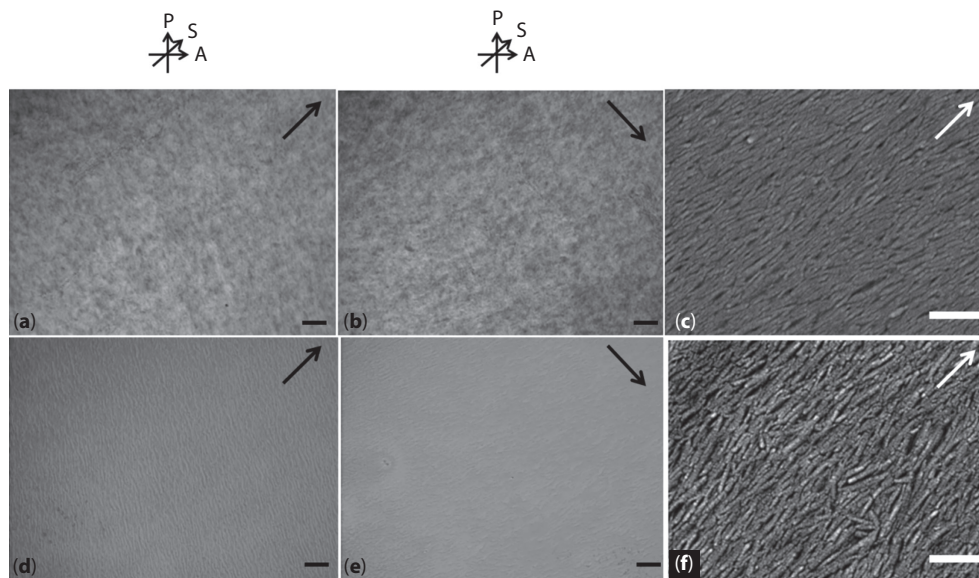


Figure 3 CNC spin-coated films: (a–c) 147 mg/ml and 2500 rpm and (d–f) 93 mg/mL and 4000 rpm. (a,b,d,e) Images viewed with reflective polarized microscopy and first-order retardation plate. Axis P is the polarizer optical axis; Axis A is the analyzer optical axis; Axis S is the first-order retardation plate slow optical axis (blue color). Scale bar for images a, b, d, and e is 200 μm ; c and f are SEM images of the film's upper surface with 500 nm scale bar. The arrow in the image denotes the radial direction.

oriented radially from a point at the center of the sample because of the shearing action on the fluid during spin coating. At 93 mg/ml, the film viewed through a cross-polarized microscope (first-order retardation plate attached) shows little color contrast as the sample stage is rotated 90° (Figure 3d,e). The SEM images (Figure 3c,f) indicate a high degree of nanorod orientation on the film surface in the radial direction of the spin flow. The reason that 93 mg/ml film shows little birefringent color contrast at different angles could be that its film thickness is too low (<40 nm) to obtain enough birefringence intensity that can be captured by the microscope.

Despite the uniform surface with high orientation order, bulk view and optical profilometry reveal that some films have pronounced striation features that include radial ridges oriented in the direction of the flow and ripple structures that appear as rings: i.e., tangentially surface undulation structures with a typical periodicity and average peak-to-valley height. Figure 4 shows one example (CNC film made from CNC suspension with 147 mg/ml and 2000 rpm rotational speed) that has both a low surface roughness area in the center and the rippled pattern emerging mid-way along the wafer radius to the edge. Depending on the feature size, the striation patterns are not always distinguishable by the naked eye and require higher magnification and measurement with optical profilometry. The striation patterns are detected for the 125 mg/ml films above 3000 rpm, 147 mg/ml above 5000 rpm, and 172 mg/ml above 2000 rpm (shown in Figure 5). At 125 mg/ml and 2000 rpm a cellular-like pattern of surface dimples is observed in the center area of the film (Figure 5a,g). This pattern is suggestive of Bénard convection cells, which are regular surface undulations that arise due to convection rolls that establish as a result of buoyancy and thermocapillary effects [26]. Capillary forces that drive convection can be generated by compositional gradients. The CNC

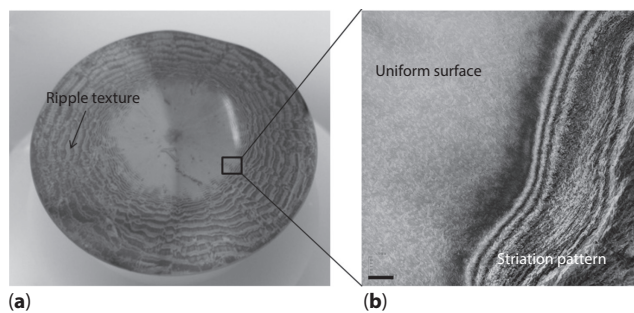


Figure 4 (a) Image of spin-coated CNC film for 147 mg/ml and 2000 rpm; (b) magnified image of the boundary between the uniform surface and striation pattern texture viewed with optical profilometer; scale bar is 50 μm .

suspension experiences extensive shear flow along the radius direction during spin coating (causing thickness reduction), therefore stable cellular patterns will not develop over the entire spinning film. Still, gradients in surface tension will develop due to evaporative cooling and water depletion, which results in similar processes within the spin-coated film as higher surface

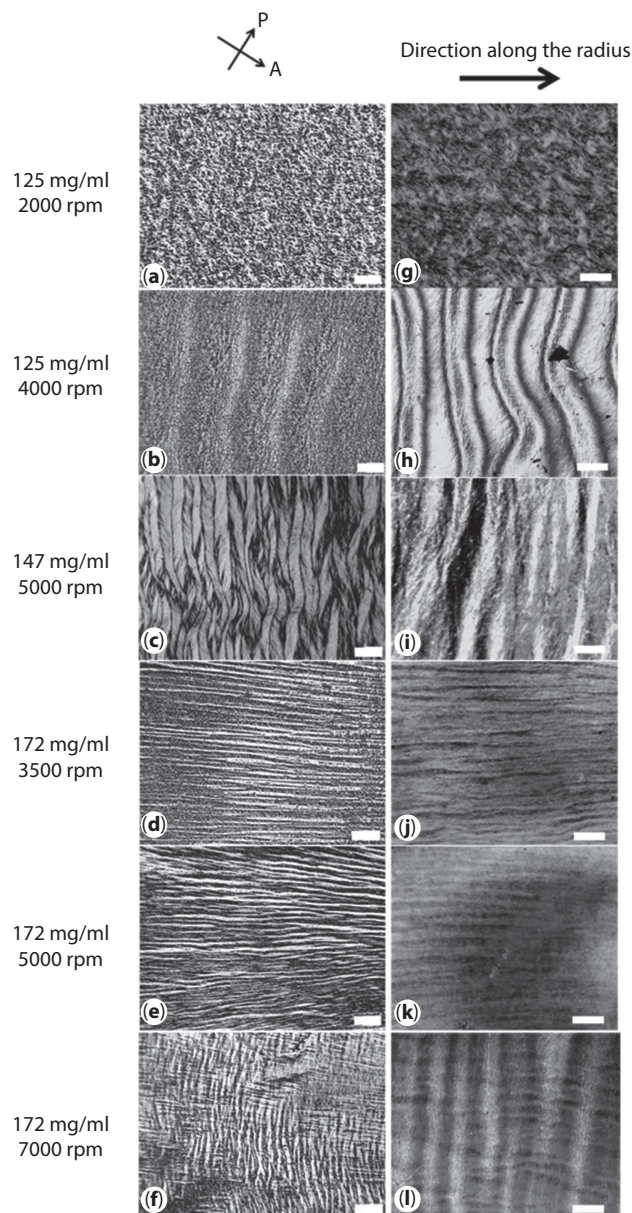


Figure 5 (a–f) Cross-polarized microscope images of CNC spin-coated film: (a,c–f) scale bar is 100 μm ; (b) scale bar is 200 μm . (g–i) Optical profilometry images of CNC spin-coated film showing the striation patterns: (g,i–l) scale bar is 50 μm ; (b) scale bar is 100 μm . The film processing conditions are listed on the left. Axis P is the polarizer optical axis; Axis A is the analyzer optical axis. For all images, the radial shear direction is horizontal left to right.

tension regions draw fluid away from lower surface tension regions. Thus, the localized fluid thickness modulation that results in the cellular pattern at the substrate center becomes stretched and interconnected at higher spin speeds due to bulk fluid flow at regions away from the wafer center. The stretching phenomena of this cellular pattern produces what eventually become the striations. Two types of striation are captured in this experiment. The ridges (Figure 5d,e,j,k) observed in the sample films are only along the radial direction while the ripples (Figure 5b,c,h,i) are long waves propagating in the radial direction. Interestingly, the radial ridges appear from the center, however, the ripples emerge midway from the wafer center. At high concentration and high rotational speed (172 mg/ml above 7000 rpm Figure 5f,i), both radial ridges and ripples are simultaneously observed and overlap.

The periodical surface structure is observed using both optical profilometry and cross-polarized microscopy, as shown in Figure 5. The striation structure in Figure 5b (125 mg/mL and 4000 rpm) shows an interference color-band texture. This can be correlated with the thickness difference on the surface of the striation, which will be discussed in the following paragraph. Higher magnification of the same film in Figure 6 revealed more details of the CNC orientation and structure, where a periodical band-like thread texture is observed. Brightness and optical pattern appearance as the stage is rotated with respect to the polarized optical axis indicates an oriented structure formation. The striation pattern in Figure 5c,i (147 mg/mL and 5000 rpm) also shows this band-like thread texture. The pairs of dark bands almost fuse as the stage is rotated 90° with respect to the polarized optical axis, which is similar to the precholesteric bands birefringence texture observed in concentrated procollagen solution by Martin *et al.* [33]. The addition of a first-order retardation plate yields blue and orange bands in Figure 6c,d. This suggests that the CNC rods lie oblique to the direction of the bands and that their orientation changes from one band to the other. This could be attributed to the process of compaction and sliding of prealigned (by spin flow shear force) nanorods in concentrated CNC suspension.

In order to correlate the striation structure dimensions, the average height of irregularities, R_z , and average spacing of local peaks, S , were measured, representing the height and spacing of striations, respectively. The measurement results are presented in Tables 3–5. The ripple pattern is only observed in a narrow range of rotational speeds, which increases with increasing concentration. At a given concentration, higher rotational speeds resulted in both a decreased lateral spacing (S) between the ripples and a decreased average height of the ripples (R_z), which indicates a smoothing of the wrinkles as the rotational speed increases. When the rotational speed is fixed, a decrease of S is observed with increasing concentration, which indicates an increased propensity for ripples at higher viscosities. The radial ridges were only observed at the highest concentration, 172 mg/ml, but at all rotational speeds above 2000 rpm. The dimension of the radial ridges follows the same trend as the ripples, with a decreased lateral spacing (S) and a decreased average height (R_z) with higher rotational speeds. Furthermore, the ripple structure has a

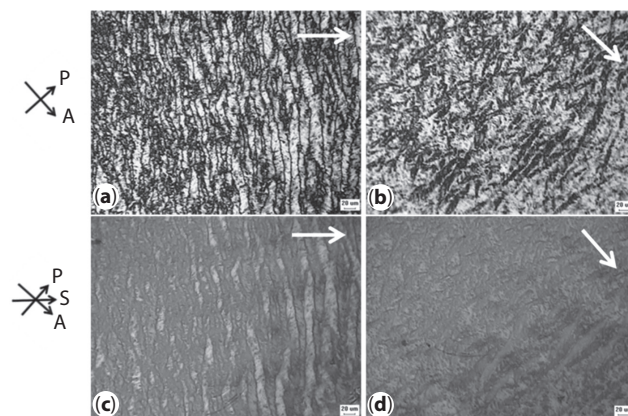


Figure 6 Polarized microscopy images of CNC film without (a,b) and with first-order retardation plate (c,d). Film processing conditions are 125 mg/mL suspension and 5000 rpm rotational speed. All scale bars are 20 μm . (a,c) 20X images with the radial direction at 45° from the polarizer optical axis. (b,d) 20X image with the radial direction at 90° from the polarizer optical axis.

Table 3 Average spacing of the surface ripples in the CNC films. Dashes indicate no observed ripples.

Concentration	Rotational speed				
	2000 rpm	4000 rpm	5000 rpm	7000 rpm	8000 rpm
125 mg/ml	–	>1 mm	151 μm	–	–
147 mg/ml	–	–	100 μm	40.7 μm	–
172 mg/ml	–	–	–	5.30 μm	5.40 μm

Table 4 Average height of the surface ripples in the CNC films. Dashes indicate no observed ripples.

Concentration	Rotational speed				
	2000 rpm	4000 rpm	5000 rpm	7000 rpm	8000 rpm
125 mg/ml	–	0.31 μm	0.20 μm	–	–
147 mg/ml	–	–	0.41 μm	0.32 μm	–
172 mg/ml	–	–	–	0.20 μm	0.07 μm

Table 5 Average spacing and height of the radial ridges for the CNC films. Dashes indicate no observed striations.

	Rotational speed				
	2000 rpm	4000 rpm	5000 rpm	7000 rpm	8000 rpm
Average Spacing	–	85.7 μm	82.6 μm	77.7 μm	32.5 μm
Average Height	–	0.22 μm	0.10 μm	0.05 μm	0.03 μm

relatively larger range of S (5 to 1000 μm) compared to radial ridges (32 to 85 μm).

In order to understand these phenomena, the striation formation model has to be addressed. Scriven [34] proposed that a spin-coating process consists of four successive steps; deposition, spin-up, spin-off and evaporation. The striation formation takes place in the solvent evaporation step by one explanation. This explanation is based on the Marangoni effect, which is the collective name for composition-gradient-driven capillary effects [35, 36]. However, it is not quite clear if the evaporation step is really the decisive and only step where striations are formed. In the case of Marangoni instability resulting from thermocapillary or solutocapillary forces, a “Marangoni number,” M_n , was devised by Pearson in 1958 [36]. For the CNC spin-coating process, the film thickness may not be sufficiently large for inducing the stable thermocapillary convection. Birnie [27] pointed out that the solutocapillary flow induced by concentration gradients is more important than the thermocapillary flow caused by temperature gradients. Thus, all spin-coating processes here are at room temperature and thermal gradients are not a variable parameter. Since the driving force is imposed by a composition gradient rather than a temperature gradient, M_n in Equation 2 is used to evaluate the significance of solvent gradient effects upon the development of convection cells [37]:

$$M_n = \frac{\left(\frac{\partial\sigma}{\partial C}\right)H^2\nabla C}{\eta D} \quad (2)$$

where $\frac{\partial\sigma}{\partial C}$ is the change in surface tension with concentration, H is the fluid thickness, C is the relevant composition variable, D is the diffusion rate of the

component driving the composition-dependent surface tension change, and η is the viscosity.

According to Equation 2, lower thicknesses and higher solution viscosities, η , can suppress evolution of striations through decreased M_n . Higher substrate rotation speeds were shown by their calculation to reduce M_n through decreased film thickness, H , and were predicted to suppress striation formation, which agrees with our experimental results for both radial ridges and ripple rings. The M_n should be proportional to the film thickness in the model. Although both the average spacing and average height of the striation shows decreasing of its amplitude as the rotation speed increases, the film thickness does not show a good linear trend with the decrease striation dimension as shown in Figure 7 (only for radial ridges). This indicates that the film thickness is not the single dominating parameter in the striation formation. The model also predicts that higher solution viscosities, η , can suppress evolution of striations through decreased M_n . The higher concentration leads to a higher viscosity of the solution. However, the higher concentrations do not show a suppression of the striation (only for surface ripples), but a strengthened formation. When striation formation is explained on the basis of the Marangoni effect, striations are assumed to be formed during the water evaporation step. However, it is not quite clear if the evaporation step is really the deterministic and sole step where striations are formed. Flow characteristics including viscosity of suspension, for instance, can possibly affect development of the film surface morphologies on spin-up step. Moreover, due to the non-Newtonian fluid dynamics of the CNCs solution, the shear thinning viscosity further complicates mechanistic modeling and feature size prediction.

3.3 Mechanical Properties of CNC Films

Hoeger *et al.* [12] applied a nanoindentation-based method to measure the elastic transverse modulus to be 8.3 ± 0.9 GPa for CNC films (from Ramie fibers), which is of the same order of magnitude as values predicted by molecular modeling and also reported for the single CNCs measured using AFM (e.g., 11–57 GPa and 18–50 GPa respectively) [1]. The hardness of CNC films was found to be in the range of 380 ± 30 MPa. However, the radius of curvature of the Berkovich

tip used is ≈ 50 nm, which is greater than the average CNC width (6.5 ± 0.7 nm for the CNCs from Ramie fibers). The deformation of the nanoindentation method employed in this study not only involves one single CNC, but several CNCs together. Thus, due to the size of a single Berkovich tip indentation, the measurement results are more representative of the bulk modulus of the film. The mechanical response of the film without heat treatment in our experiment is very close in value to the results of Hoeger *et al.* The moduli of the films (147 mg/mL, 2000 rpm) are 8.3 ± 0.8 and 7.8 ± 0.79 GPa and the hardness is 322 ± 36 and 283 ± 26 MPa, for rotational speeds of 2000 and 2500 rpm, respectively. The CNC film of Hoeger *et al.* has multiple layers with applied PEI coating for adhesion enhancement, but the enhancement does not appear to influence the mechanical property. It is reported that completely protonated acid form of CNCs would form stronger intermolecular hydrogen bonding between crystallites with reduced residual moisture in the CNCs film [38]. In order to promote hydrogen bonding, the dried films were subjected to post-spinning heat treatment at 80°C in an oven for 40 minutes, prior to nanoindentation measurements. By comparing the film weight difference before and after heat treatment (Table 6), there is no significant change, suggesting an absence of residual water and likely removal of bound water. This is also a demonstration of the effective drying step during spin coating. In response to the heat treatment, an approximate 2 GPa increase in modulus and 100 MPa increase in hardness were observed. It should be noted that heating above 80°C resulted in decomposition, which is indicated by the color of the film turning brown.

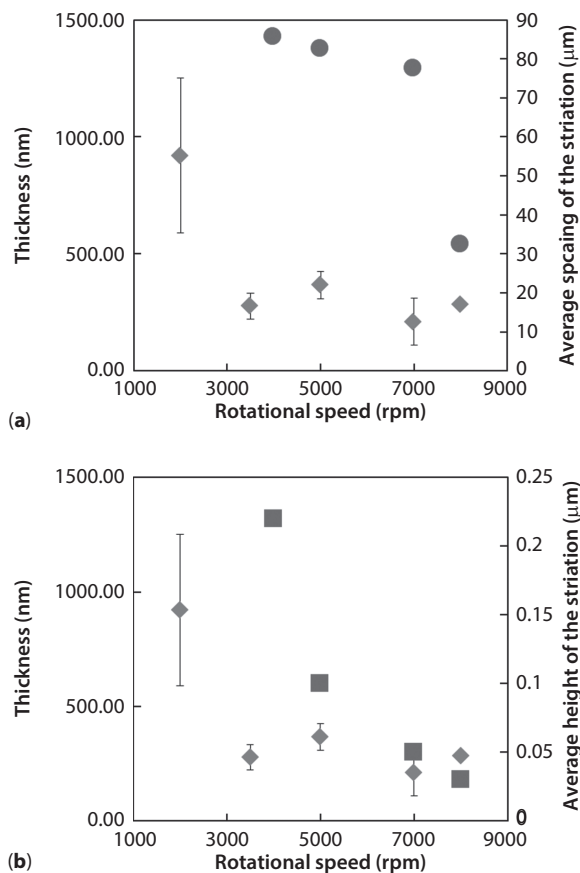


Figure 7 (a) Film thickness (diamonds) and average spacing (solid circles) of the striation (radial ridges) vs. rotational speeds. (b) Film thickness (diamonds) and average height (squares) of the striation (radial ridges) vs. rotational speeds. Films are processed at CNC concentrations of 172 mg/mL.

4 CONCLUSION

Spin coating has been used to cast uniform CNC films of thicknesses from 40 nm to 1 μm , which provides reference for industrial level CNCs-based film processing, such as microelectromechanical systems (MEMS) device manufacture. Several fundamental parameters (rotational speed and wetting film concentration) are included in the basic spin-coating model for the film thickness and roughness control. Formation of

Table 6 Mechanical properties of CNC films measured by nanoindentation.

	Sample	Thickness (nm)	Modulus (GPa)	Hardness (MPa)	Weight (mg)
Spun-dried only	147 mg/mL, 2000 rpm	793	7.8 ± 0.8	322 ± 36	5.21
	147 mg/mL, 2500 rpm	670	8.3 ± 0.8	283 ± 26	3.64
Heated Dried	147 mg/ml, 2000 rpm	793	10.9 ± 1.0	404 ± 36	5.21
	147 mg/ml, 2500 rpm	670	10.0 ± 0.4	434 ± 20	3.63

striation patterns that include both ripples and radial ridges associated with film drying instability are observed and the structural dimensions correlate with the spin parameters. Due to the liquid crystal nature of CNT, the radial orientation of nanorods induced by spinning shear flow has been found in the uniform film surface. The striation structure also comes with periodical band-like birefringent textures, captured by polarized light microscopy. Potential exists for low-cost and automatic formation of surface patterns that may be integral in the development of polymer semiconductor devices such as integrated circuits and display elements. Also, the unique birefringent texture of this striation structure might broaden the application of these anisotropic nanorod films into the optical components field, such as diffraction gratings. Mechanical properties of the films have been measured using nanoindentation. The maximum elastic modulus of the films was 8.3 GPa and the maximum hardness was 322 MPa. By conducting a post-spinning heat treatment (80 °C), we observed a 17% increase in modulus and a 35% increase in hardness, which are attributed to the stronger intermolecular hydrogen bonding between crystallites with complete removal of water.

REFERENCES

1. R.R. Lahiji, X. Xu, R. Reifengerger, A. Raman, A. Rudie, and R.J. Moon, Atomic force microscopy characterization of cellulose nanocrystals. *Langmuir* **26**, 4480–4488 (2010).
2. R.J. Moon, A. Martini, J. Nairn, J. Simonsen, and J. Youngblood, Cellulose nanomaterials review: Structure, properties and nanocomposites. *Chem. Soc. Rev.* **40**, 3941–3994 (2011).
3. E.E. Ureña-Benavides, G. Ao, V.A. Davis, and C.L. Kitchens, Rheology and phase behavior of lyotropic cellulose nanocrystal suspensions. *Macromolecules* **44**, 8990–8998 (2011).
4. W.R. Ashurst, V.A. Davis, and C.L. Kitchens, Microdevices and Methods of Manufacture. US Patent 2014/0044937 A1, (Feb. 13, 2014).
5. B. Sun and H. Sirringhaus, Surface tension and fluid flow driven self-assembly of ordered ZnO nanorod films for high-performance field effect transistors. *J. Am. Chem. Soc.* **128**, 16231–16237 (2006).
6. K. Norrman, A. Ghanbari-Siahkali, and N. Larsen, 6 Studies of spin-coated polymer films. *Annu. Rep. Sect. "C" (Phys. Chem.)* **101**, 174–201 (2005).
7. B. Schyrr, S. Pasche, G. Voirin, C. Weder, Y.C. Simon, and E.J. Foster, Biosensors based on porous cellulose nanocrystal-poly (vinyl alcohol) scaffolds. *ACS Appl. Mater. Interfaces* **6**, 12674–12683 (2014).
8. Y. Zhou, C. Fuentes-Hernandez, T.M. Khan, J.C. Liu, J. Hsu, J.W. Shim, *et al.*, Recyclable organic solar cells on cellulose nanocrystal substrates. *Sci. Rep.* **3**, 1536 (2013).
9. E.D. Cranston and D.G. Gray, Birefringence in spin-coated films containing cellulose nanocrystals. *Colloids Surf., A* **325**, 44–51 (2008).
10. E. Kontturi, L.S. Johansson, K.S. Kontturi, P. Ahonen, P.C. Thüne, and J. Laine, Cellulose nanocrystal sub-monolayers by spin coating. *Langmuir* **23**, 9674–9680 (2007).
11. H.T. Winter, C. Cerclier, N. Delorme, H. Bizot, B. Quemener, and B. Cathala, Improved colloidal stability of bacterial cellulose nanocrystal suspensions for the elaboration of spin-coated cellulose-based model surfaces. *Biomacromolecules* **11**, 3144–3151 (2010).
12. I. Hoeger, O.J. Rojas, K. Efimenko, O.D. Velev, and S.S. Kelley, Ultrathin film coatings of aligned cellulose nanocrystals from a convective-shear assembly system and their surface mechanical properties. *Soft Matter* **7**, 1957–1967 (2011).
13. J.A. Diaz, X. Wu, A. Martini, J.P. Youngblood, and R.J. Moon, Thermal expansion of self-organized and shear-oriented cellulose nanocrystal films. *Biomacromolecules* **14**, 2900–2908 (2013).
14. Y. Habibi, L. Foulon, V. Aguié-Béghin, M. Molinari, and R. Douillard, Langmuir–Blodgett films of cellulose nanocrystals: Preparation and characterization. *J. Colloid Interface Sci.* **316**, 388–397 (2007).
15. D.B. Hall, P. Underhill, and J.M. Torkelson, Spin coating of thin and ultrathin polymer films. *Polym. Eng. Sci.* **38**, 2039–2045 (1998).
16. S.A. Jenekhe, The rheology and spin coating of polyimide solutions. *Polym. Eng. Sci.* **23**, 830–834 (1983).
17. S.A. Jenekhe and S.B. Schuldt, Coating flow of non-Newtonian fluids on a flat rotating disk. *Ind. Eng. Chem. Fundam.* **23**, 432–436 (1984).
18. B. Washo, Rheology and modeling of the spin coating process. *IBM J. Res. Dev.* **21**, 190–198 (1977).
19. X. Min, X. Orignac, and R.M. Almeida, Striation-free, spin-coated sol-gel optical films. *J. Am. Ceram. Soc.* **78**, 2254–2256 (1995).
20. D. Meyerhofer, Characteristics of resist films produced by spinning. *J. Appl. Phys.* **49**, 3993–3997 (1978).
21. T.J. Rehg and G. Higgins, Spin coating of colloidal suspensions. *AIChE J.* **38**, 489–501 (1992).
22. C. Lawrence and W. Zhou, Spin coating of non-Newtonian fluids. *J. Non-Newtonian Fluid Mech.* **39**, 137–187 (1991).
23. H. Kozuka, Y. Ishikawa, and N. Ashibe, Radiative striations of spin-coating films: Surface roughness measurement and in-situ observation. *J. Sol-Gel Sci. Technol.* **31**, 245–248 (2004).
24. P. Mokarian-Tabari, M. Geoghegan, J.R. Howse, S.Y. Heriot, R.L. Thompson, and R.A.L. Jones, Quantitative evaluation of evaporation rate during spin-coating of polymer blend films: Control of film structure through defined-atmosphere solvent-casting. *Eur. Phys. J. E Soft Matter* **33**, 283–289 (2010).
25. D.E. Haas, J.N. Quijada, S.J. Picone, and D.P. Birnie III, Effect of solvent evaporation rate on skin formation during spin coating of complex solutions. *Proc. SPIE* **3943**, 280–284 (2000).

26. M.J. Block, Surface tension as the cause of Bénard cells and surface deformation in a liquid film. *Nature* **178**, 650–651 (1956).
27. D.P. Birnie, Rational solvent selection strategies to combat striation formation during spin coating of thin films. *J. Mater. Res.* **16**, 1145–1154 (2001).
28. A. Vidal and A. Acrivos, Effect of nonlinear temperature profiles on onset of convection driven by surface tension gradients. *Ind. Eng. Chem. Fundam.* **7**, 53–58 (1968).
29. M. Sprenger, S. Walheim, C. Schäfle, and U. Steiner, Hierarchical pattern replication by polymer demixing. *Adv. Mater.* **15**, 703–706 (2003).
30. W.C. Oliver and G.M. Pharr, An improved technique for determining hardness and elastic modulus using load and displacement sensing indentation experiments. *J. Mater. Res.* **7**, 1564–1583 (1992).
31. N. Sahu, B. Parija, and S. Panigrahi, Fundamental understanding and modeling of spin coating process: A review. *Indian J. Phys.* **83**, 493–502 (2009).
32. T. Ebeling, M. Paillet, R. Borsali, O. Diat, A. Dufresne, J.Y. Cavaille, and H. Chanzy, Shear-induced orientation phenomena in suspensions of cellulose microcrystals, revealed by small angle X-ray scattering. *Langmuir* **15**, 6123–6126 (1999).
33. R. Martin, J. Farjanel, D. Eichenberger, A. Colige, E. Kessler, D.J. Hulmes, and M.M. Giraud-Guille, Liquid crystalline ordering of procollagen as a determinant of three-dimensional extracellular matrix architecture. *J. Mol. Biol.* **301**, 11–17 (2000).
34. L. Scriven, Physics and applications of dip coating and spin coating, in *MRS Proceedings* **121**, 717–729, Cambridge University Press (1988).
35. J. Pearson, On convection cells induced by surface tension. *J. Fluid Mech.* **4**, 489–500 (1958).
36. L. Scriven and C. Sternling, The Marangoni effects. *Nature* **187**, 186–188 (1960).
37. D.E. Haas and D.P. Birnie III, Evaluation of thermo-capillary driving forces in the development of striations during the spin coating process. *J. Mater. Sci.* **37**, 2109–2116 (2002).
38. S. Beck, J. Bouchard, and R. Berry, Dispersibility in water of dried nanocrystalline cellulose. *Biomacromolecules* **13**, 1486–1494 (2012).